An Analytical Model of Active Layer Depth under Changing Ground Heat Flux

Modi ZHU[1], Jingfeng Wang[1], Valeriy Yuryevich Ivanov[2], Aleksey Y Sheshukov[3], Wenbo Zhou[2], Liujing Zhang[4], Valeriy Mazepa[5], Alexandr Sokolov[6], and Victor Valdayskikh[7]

[1]Georgia Institute of Technology
[2]University of Michigan-Ann Arbor
[3]Kansas State University
[4]University of Michigan
[5]Russian Academy of Sciences-Ural Branch
[6]Institute of Plant and Animal Ecology, the Ural Branch of the Russian Academy of Sciences, Arctic Research Station
[7]Unknown

June 23, 2023

Abstract

A physically based analytical model is formulated to simulate the thaw depth of active layer under changing boundary condition of soil heat flux. The energy conservation statement leads to a nonlinear integral equation of the thaw depth using an approximate temperature profile as an analytical solution of the diffusion equation describing the heat transfer in the active layer. The time-varying soil surface heat flux is estimated using non-gradient models when field observations are not available. The proposed model was validated against field observations at three Arctic forest and tundra sites. The simulated thaw depth and soil temperature profiles are in good agreement with observations hinting the potential for model application at larger spatial scales.

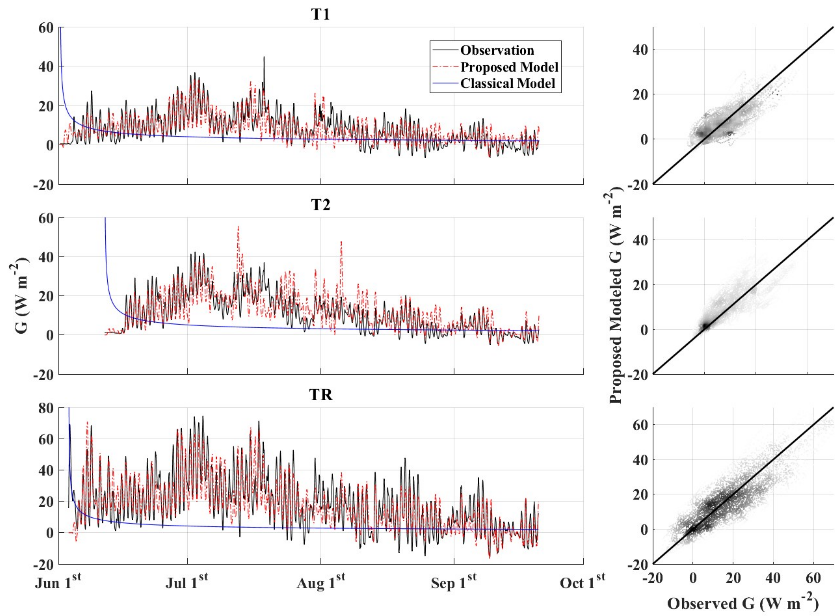
T1
T2
TR
Observation
Proposed Model
Classical Model
G (W m^{-2})
Jun 1st
Jul 1st
Aug 1st
Sep 1st
Oct 1st
Proposed Modeled G (W m^{-2})
Observed G (W m^{-2})

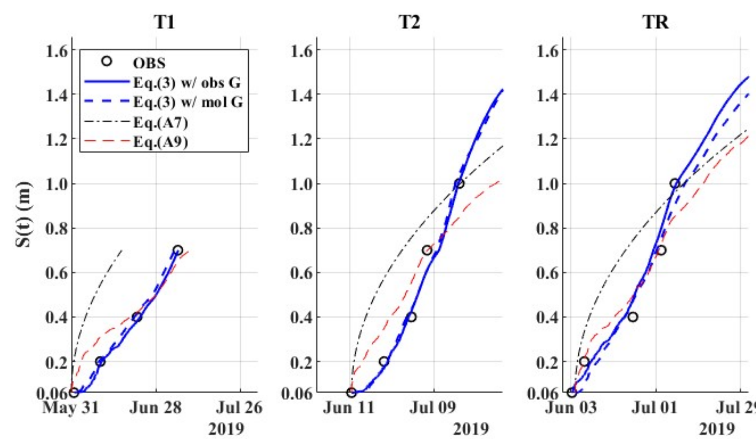
T1
T2
TR
OBS
Eq.(3) w/ obs G
Eq.(3) w/ mol G
Eq.(A7)
Eq.(A9)
S(t) (m)
May 31
Jun 28
Jul 26
2019
Jun 11
Jul 09
2019
Jun 03
Jul 01
Jul 29
2019

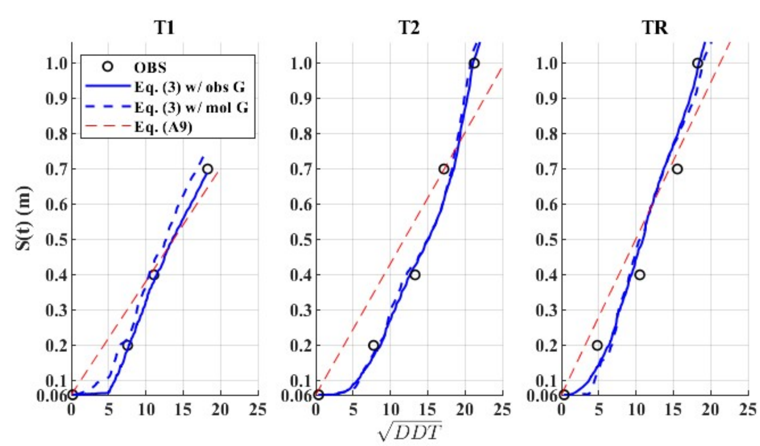
T1
T2
TR
OBS
Eq. (3) w/ obs G
Eq. (3) w/ mol G
Eq. (A9)
S(t) (m)
$\sqrt{DDT}$

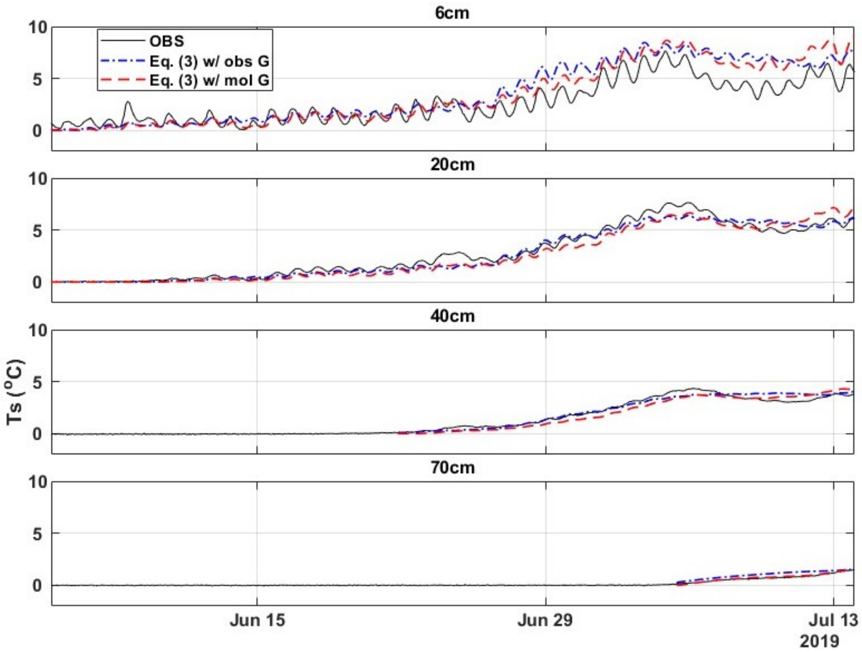
6cm
20cm
40cm
70cm
OBS
Eq. (3) w/ obs G
Eq. (3) w/ mol G
Ts (°C)
Jun 15
Jun 29
Jul 13
2019

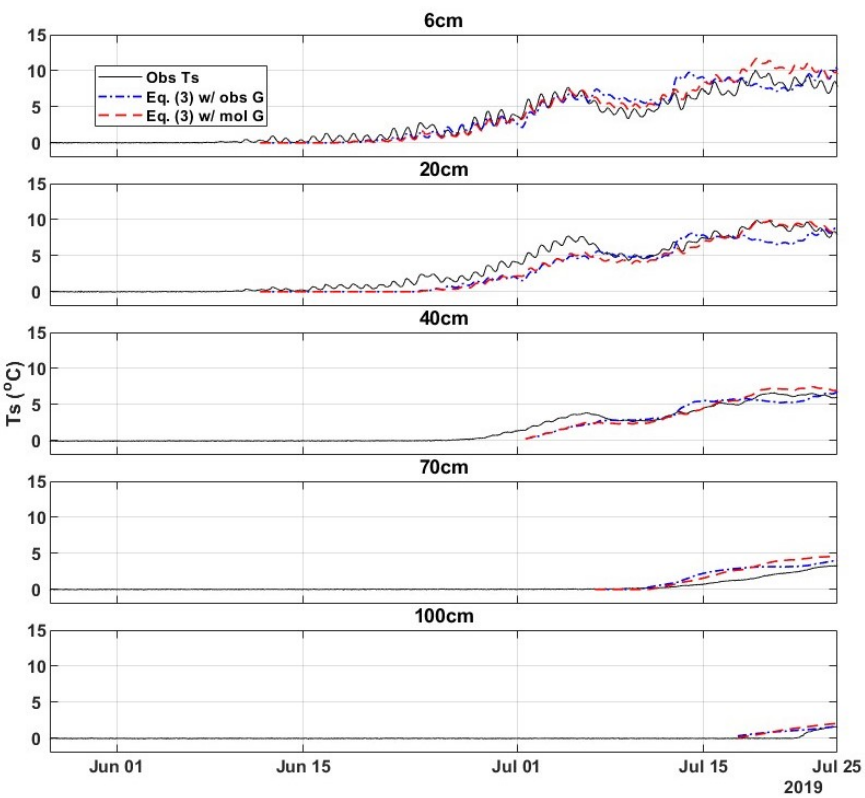
6cm
20cm
40cm
70cm
100cm
Obs Ts
Eq. (3) w/ obs G
Eq. (3) w/ mol G
Ts (°C)
Jun 01
Jun 15
Jul 01
Jul 15
Jul 25
2019

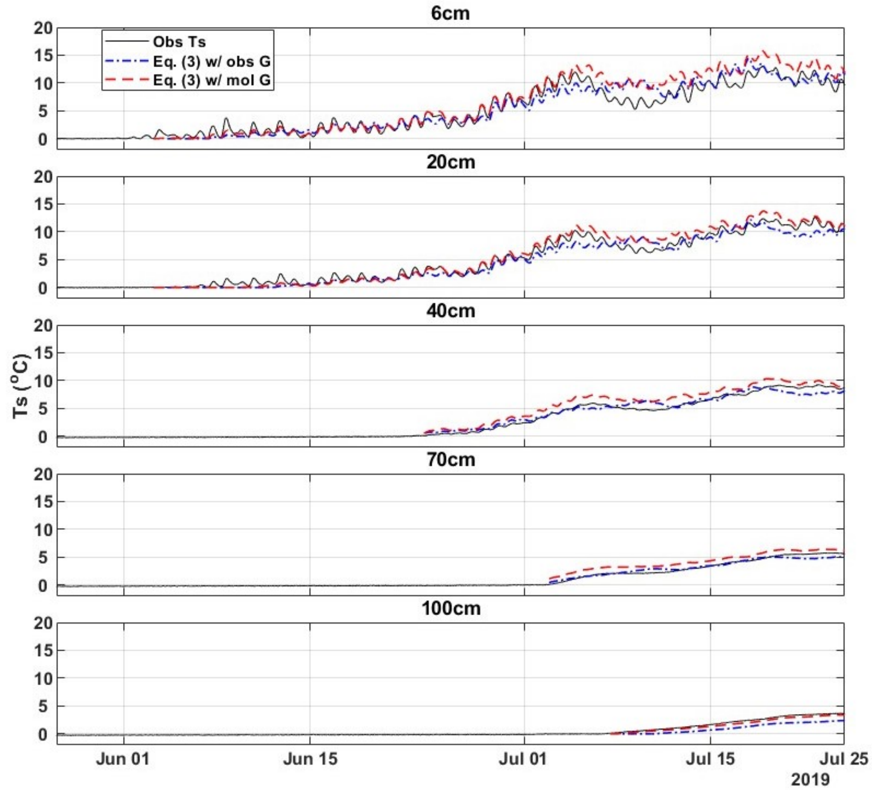
6cm
20
15
10
5
0
Obs Ts
Eq. (3) w/ obs G
Eq. (3) w/ mol G
20cm
40cm
Ts (°C)
70cm
100cm
Jun 01
Jun 15
Jul 01
Jul 15
Jul 25
2019

An Analytical Model of Active Layer Depth under Changing Ground Heat Flux

Modi Zhu[1], Jingfeng Wang[1], Valeriy Ivanov[2], Aleksey Sheshukov[3], Wenbo Zhou[2], Liujing Zhang[2], Valeriy Mazepa[4], Alexandr Sokolov[5], Victor Valdayskikh[6]

[1]School of Civil and Environmental Engineering, Georgia Institute of Technology, U.S.A.
[2]Department of Civil and Environmental Engineering, University of Michigan, U.S.A.
[3]Department of Biological and Agricultural Engineering, Kansas State University, U.S.A.
[4]Institute of Plant and Animal Ecology, the Ural Branch of the Russian Academy of Sciences, Yekaterinburg, Russia
[5]Arctic Research Station, Institute of Plant and Animal Ecology, the Ural Branch of the Russian Academy of Sciences, Labytnangi, Russia
[6]Ural Federal University, Yekaterinburg, Russia

Key Points:

- The proposed model is highly effective in modeling thawing depth at higher time resolution and representing the soil energy budget.
- Non-gradient models demonstrate a strong capability to model soil energy budget in data-sparse harsh environments.

Corresponding author: Modi Zhu, `modizhu@gatech.edu`

Corresponding author: Jingfeng Wang, `jingfeng.wang@ce.gatech.edu`

Abstract

A physically based analytical model is formulated to simulate the thaw depth of active layer under changing boundary condition of soil heat flux. The energy conservation statement leads to a nonlinear integral equation of the thaw depth using an approximate temperature profile as an analytical solution of the diffusion equation describing the heat transfer in the active layer. The time-varying soil surface heat flux is estimated using non-gradient models when field observations are not available. The proposed model was validated against field observations at three Arctic forest and tundra sites. The simulated thaw depth and soil temperature profiles are in good agreement with observations hinting the potential for model application at larger spatial scales.

Plain Language Summary

An analytical model considering soil energy budget is developed to predict the thaw depth of permafrost in Arctic regions. When field data is unavailable, alternative models are applied to estimate the soil surface heat flux. The validation of this model across three Arctic forest and tundra sites has revealed a high degree of accuracy in its simulated thaw depth and soil temperature profiles compared to field observations. These results suggest the model's potential for future applications at broader spatial scales.

1 Introduction

The enhanced warming rates of Arctic regions over the past decades (ACIA, 2004; Bekryaev et al., 2010; Chapin et al., 2005; Overpeck et al., 1997; Serreze et al., 2000) have stimulated active research on permafrost dynamics (e.g. Jorgenson et al., 2006; Oelke et al., 2003; V. E. Romanovsky et al., 2010; Yi et al., 2018). There is a high interest to further our understanding of the effect of increasing surface temperatures on the freeze-thaw cycles in the ground surface layer in which the water phase seasonally alternates between liquid and solid – commonly referred to as the 'active layer'. Moreover, recent studies have been shifting the emphasis of modeling thermodynamic processes from the annual to sub-daily time scales (e.g. Bui et al., 2020; Evans & Ge, 2017; Riseborough et al., 2008; Walvoord & Kurylyk, 2016). These time scales permit improved process understanding of how climate change can impact the seasonality and variability of the active layer dynamics. Such understanding is crucial for the livelihoods of communities who rely on the state of the ground for transportation or animal husbandry (Crate et al., 2017). This knowledge is also of utmost importance for understanding the dynamics of the biogeochemical processes in Arctic soils as seasonal swings to above freezing temperatures leads to the substantial enhancement of decomposition rates of the accumulated carbon stocks (Schuur et al., 2015). The maximum depth of seasonal thaw penetration also informs engineering decisions related to infrastructure in the Arctic (Streletskiy et al., 2012).

While the physics of freeze-thaw processes has been extensively studied (e.g. Miller, 1980), analytical treatment of the related problems has remained limited. Analytical solutions of heat conduction in porous media under various initial and boundary conditions are well-developed for cases without water phase change (e.g. Carslaw & Jaeger, 1947; Crank, 1975). Developing analytical solutions of thaw depth has been challenging primarily due to the strong nonlinearity of the governing equation caused by the thawing front as a moving boundary of the solution domain. The typical for natural environments temporal variation of the surface boundary conditions of temperature or heat flux also complicates the derivation of analytical solutions of the heat transfer equation.

Problems involving a moving freeze-thaw boundary are called Stefan problems (Vuik, 1993). The traditional models of freeze-thaw processes in porous media are formulated based on the two-phase (liquid and solid water) Stefan problem, aiming to resolve the thaw depth with constant temperature boundary condition applied at the surface of a semi-infinite soil column (e.g. Alexiades, 1992; Lunardini, 1981) (Appendix A). Common assumptions postulate that (a) temperature distribution of the water liquid phase is described by a heat diffusion equation (A1), and (b) the temperature of the water solid (ice) phase remains constant at the melting point (e.g. Lunardini, 1981). The rate of solid-to-liquid phase change at the thawing front and equal to the conductive heat flux, known as the Stefan condition, is imposed as the boundary condition at thawing front (A3).

The two-phase Stefan problem is strongly nonlinear due to the moving thawing front, whose location needs to be found as part of the solution. The analytical solution of temperature and thawing front location of the Stefan problem, referred to as the "Neumann similarity solution" or the "Neumann solution" (A4, A5), predicts that the thaw depth location is proportional to the square root of time since the onset of thaw process. Under certain conditions of the physical parameters (i.e., heat capacity of liquid water and latent heat of fusion), the Neumann solution becomes the Stefan solution (Lunardini, 1981) in which the thaw depth becomes a function of the constant surface temperature (A7). To our knowledge, an analytical solution of temperature and thaw depth under temporally changing surface temperature condition does not exist. Therefore, analytical models of the thawing front based on the classical two-phase Stefan problem do not capture the effect of changing surface temperature and/or soil heat flux on the thaw depth – which are more realistic conditions of seasonal thaw. A modified Stefan solution (Ladanyi & Andersland, 2004; Lunardini, 1981) for the estimation of active layer thickness (ALT) uses the degree-days thawing (DDT) index (Van Everdingen, 1998). This modified Stefan solution has been shown to outperform the classical solution in modeling active layer freeze-thaw cycles at the annual scale (e.g. K. M. Hinkel & Nicholas, 1995; Nelson et al., 1997). However, it cannot accurately simulate thaw depth at the sub-daily time scales due to neglect of soil surface energy conservation and time-varying soil properties such as thermal conductivity and diffusivity (K. M. Hinkel & Nicholas, 1995).

In natural environments, surface temperature and ground heat flux vary diurnally and seasonally and therefore there are both theoretical and practical needs to advance analytical solutions that can capture such a variability. For example, a semi-empirical solution of the Stefan Problem at the annual scale was proposed by assuming the sinusoidal seasonal variation of air temperature (Kudryavtsev et al., 1977). This semi-empirical solution was applied to estimate ALT in the coastal region of Alaska (V. Romanovsky & Osterkamp, 1997). It was found that thaw depth depends not only on the thawing index, which is defined as the cumulative number of degree-days above 0 degree Celsius for a given time, but also on the time history of surface temperature. Further application of the semi-empirical solution to ALT dynamics for the northern hemisphere (Anisimov et al., 1997) suggests that the semi-empirical model is not well constrained by the biases in evaluation of surface energy budget.

Furthermore, analytical solutions can have a prognostic value in models that resolve the coupled dynamics of land-surface energy and water budgets. The modified Stefan solution with the thawing index has been used to describe freeze-thaw cycles in the Arctic region in the coupled land-atmosphere models such as SiB2 (Sellers et al., 1996; Li & Koike, 2003), SHAW (Flerchinger, 2000), and Community Land Model, CLM (Oleson et al., 2013). It was found that the modified Stefan solution is not efficient in meeting energy budget in the thawing procedure. For example, the modified Stefan solution using thawing index in CLM over-estimates freeze/thaw depth due to ignoring soil conductive heat flux (e.g. Gao et al., 2019).

Driven by the need to improve a description of freeze-thaw dynamics under temporally varying boundary conditions, the objective of this study is to formulate an analytical model of thaw depth under the changing surface ground heat flux. This model will be applicable for the cases of sub-daily to seasonal time scale flux variations allowing to simulate freeze-thaw processes for a range of assessment scenarios.

2 Model Formulation

The conservation of energy for the active layer is expressed as

$$\int_0^{S(t)} C_s[T(x,t) - T_m]dx + \lambda_f \rho_i \int_0^{S(t)} \theta_i(x)dx = \int_0^t G(\tau)d\tau \tag{1}$$

where $S(t)$ (m) is the thaw depth at time t, $T(x,t)$ (°C) is the soil temperature with depth x, G ($\mathrm{Wm^{-2}}$) is the ground heat flux, $\theta_i(x)$ is the pre-thawing ice content profile, and τ the integration (dummy) time variable. The parameters include the bulk soil volumetric heat capacity C_s, density of ice ρ_i ($\mathrm{kgm^{-3}}$), latent heat of fusion λ_f (3.34×10^5 $\mathrm{Jkg^{-1}}$), and the melting-point of water T_m (0°C). Thawing starts when active layer reaches isothermal condition at T_m (e.g. Frauenfeld et al., 2007; Outcalt et al., 1990). The first integral on the left-hand side represents the thermal energy storage from the surface down to the thawing front, and the second term is the latent heat associated with the fusion of ice over the same depth range. The integral on the right-hand side is the total energy supply for ice melting and heat storage due to the soil surface heat flux into the active layer.

An analytical solution of $T(x,t)$ for a one-dimensional semi-infinite domain (Carslaw & Jaeger, 1947) without phase change (i.e., without accounting for the heat of fusion of ice) is

$$T(x,t) = T_0 + \frac{1}{I_s\sqrt{\pi}} \int_0^t exp\left[-\frac{x^2}{4\alpha_s(t-\tau)}\right] \frac{G(\tau)d\tau}{\sqrt{t-\tau}} \tag{2}$$

where I_s is the bulk soil thermal inertia ($\mathrm{Jm^{-2}K^{-1}s^{-1/2}}$), α_s is the bulk soil thermal diffusivity ($\mathrm{m^2s^{-1}}$), and T_0 is the initial soil temperature (°C) assumed to be uniform with depth (taken as T_m in this study). For the case of ice melting, the temperature profile during the thawing period may be represented by the temperature profile without phase change (taken as $T(x,t)$ in Eq. (2)) superimposed by a temperature correction term (taken as $-T(S(t),t)$) caused by the phase change, when liquid-ice interface is varying slowly in time (Mamode, 2013). Thawing front temperature remaining at T_m requires that $T(S(t),t) = T_m$ in Eq. (1), which implies that the temperature profile above the thawing front depth is warmer than T_m and the difference $T(x,t) - T(S(t),t)$ is positive according to Eq. (2). Substituting Eq. (2) into Eq. (1) leads to a nonlinear integral equation of $S(t)$,

$$\lambda_f \rho_i \int_0^{S(t)} \theta_i(x)dx = \int_0^t G(\tau) \left[erfc\left(\frac{S(\tau)}{2\sqrt{\alpha_s(t-\tau)}}\right) + \frac{S(\tau)}{\sqrt{\alpha_s \pi (t-\tau)}} exp\left(-\frac{S^2(\tau)}{4\alpha_s(t-\tau)}\right)\right] d\tau \tag{3}$$

where erfc is the complementary error function, and the integration lower limit $\tau = 0$ is the time when the land surface starts to thaw.

Flux G in Eqs. (1) – (3) is surface ground heat flux at the top of vertically homogeneous mineral soil subjected to freeze-thaw cycles. The application of Eq. (3) is straightforward if the time series of G are available from measurements. When such observations are unavailable, the heat flux needs to be estimated from meteorological data or soil temperature data. In the permafrost regions, the problem is complicated by the presence of a thick peat layer, i.e., a partially decomposed biomass material that usually covers mineral soil (Robinson et al., 2003). Flux G can be derived from the conductive heat flux Q at the surface of the peat layer. The maximum entropy production (MEP) model (J. Wang & Bras, 2009, 2011), which has been successfully applied to modeling surface energy budget of the Arctic permafrost (El Sharif et al., 2019), is used for modeling Q,

$$
\begin{aligned}
Q &= R_n - E - H \\
R_n &= \left[1 + B(\sigma) + \frac{B(\sigma)}{\sigma}\frac{I_s}{I_0|H|^{\frac{1}{6}}}\right] H \\
E &= B(\sigma)H \\
B(\sigma) &= 6\left(\sqrt{1 + \frac{11}{36}\sigma} - 1\right),\ \sigma \equiv \frac{\lambda^2}{c_p R_v}\frac{q_s}{T_s^2}
\end{aligned}
\tag{4}
$$

where E (Wm^{-2}) and H (Wm^{-2}) are latent and sensible heat fluxes, respectively, R_n (Wm^{-2}) is the net radiative flux, T_s (K) is the soil surface temperature, q_s is the surface specific humidity, I_s (Jm^{-2}K^{-1}s$^{-1/2}$) is the soil thermal inertia, I_0 is the "apparent thermal inertia of the air" (J. Wang & Bras, 2009), λ (2.5×10^6 Jkg^{-1}) is the latent heat of vaporization of liquid water, c_p (10^3 Jkg^{-1}K^{-1}) is the specific heat of the air at constant pressure, and R_v (461 Jkg^{-1}K^{-1}) is the gas constant of water vapor. Radiation fluxes towards the land surface are conventionally defined as positive and the signs of Q, E, and H are opposite to those of radiation fluxes.

Soil surface heat flux G at the bottom of peat layer in Eqs. (1) – (3) is expressed in terms of Q (Z.-H. Wang & Bou-Zeid, 2012; Yang & Wang, 2014).

$$
G(t) = \int_0^t erfc\left[\frac{D}{2\sqrt{\alpha_t(t-\tau)}}\right] dQ(\tau) \tag{5}
$$

where D is the depth of the peat layer (m), α_t the thermal diffusivity of the bulk peat layer material (m^2 s^{-1}), and $\tau = 0$ is the same starting time as in Eq. (3).

3 Study Sites and Field Data

Soil temperature, soil heat flux, and other meteorological variables were collected in 2019 at a moss-lichen tundra site (66°53.652'N, 66°45.881'E) and two larch forest sites (66°53.923'N, 66°45.442'E; 66°53.760'N, 66°45.623'E) on the eastern slope of Polar Urals, Yamal-Nenets Autonomous District, Russia (Ivanov et al., 2018). The three sites (labeled as 'TR (tundra)', 'T (trees)1', and 'T (trees)2') are located in the tundra-forest transitional zone of the Arctic region at the boundary of discontinuous permafrost region (Obu et al., 2019). The mean frost-free period is 94 days and the growing season lasts from mid-June to mid-August. The mean annual precipitation is 500-600 mm with about 50% in the form of snow and sleet. Moss–lichen tundra with rock outcrops and deciduous shrub communities are the dominant land covers. Two 'Trees' sites are mountain heath tundra encroached by the Siberian larch in the past 30 years. The current surface canopy cover are 50% (Trees 1) and 30% (Trees 2), 7-8 m average height, and individual trees reaching 10 m. Sensors are identical at all sites for measuring 30-min resolution soil temperature at five depths (6, 20, 40, 70, 100 cm). Surface temperature was measured using infrared radiometers (SI-111; Apogee Instruments, Inc., Logan, Utah, USA). Net radiation and shortwave radiation (single-channel NR Lite2 Net Radiometer and CMP 3 Pyranometer; Kipp and Zonen, Delft, Netherlands) were measured at 8 m ('Tundra') and 13.5 m ('Trees') heights. Soil heat fluxes were measured by soil heat flux plate (HFP01; HuksefluxUSA, Inc., Center Moriches, NY, USA) buried at 6 cm depth into mineral soil with a peat layer of varying thickness among the different sites: 8 cm at TR, 5 cm at T1, and 6 cm at T2. Soil water content and temperature were measured using multivariable time differential reflectometer (TDR) sensors (CS655; Campbell Scientific, Inc., Logan, Utah, USA).

Table 1: The volumetric ice content profile $\theta_i(x)$ at the three sites with field observations prior to the thaw period. 'NA' for site T1 indicates that ice was not present at the depth of 100 cm at this site.

Depth (cm)	Sites		
	T1	T2	TR
6	0.10	0.20	0.33
20	0.15	0.16	0.30
40	0.15	0.20	0.23
70	0.16	0.08	0.25
100	NA	0.13	0.32

The observed thaw depths are identified by the abrupt changes in the time series of liquid water content and soil temperature (Patterson & Smith, 1981). The process of active-layer thaw is strongly affected by the ice content (Brown et al., 2000). As in-situ soil ice content data do not exist, pre-thawing ice content $\theta_i(x)$ (Table 1) is estimated from the difference of pre- and post-thawing soil liquid water content (Overduin & Kane, 2006). Depth dependence of $\theta_i(x)$ is caused by soil moisture distribution at the onset of seasonal freezing and it informs water content-dependent model parameters including thermal diffusivity α_s and thermal inertia I_s (K. M. Hinkel & Nicholas, 1995; Ochsner & Baker, 2008). In this analysis, α_s is estimated by numerically solving the inverse problem (e.g. McGaw et al., 1978; Nelson et al., 1985; K. Hinkel et al., 2001) of one-dimensional heat diffusion equation:

$$\frac{dT}{dt} = \alpha_s \frac{d^2T}{dx^2} \tag{6}$$

The time derivative can be approximated as:

$$\frac{dT}{dt} = \frac{T_i^{j+1} - T_i^{j-1}}{2\Delta t} \tag{7}$$

And the space derivative can be approximated as:

$$\frac{d^2T}{dx^2} = \frac{T_i^{j-1} - 2T_i^j + T_i^{j+1}}{\Delta x^2} \tag{8}$$

where Δt and Δx are time and space resolutions, taken as 1 hour and 0.2 m respectively. The inversely estimated diffusivities α_s at the three studied sites are summarized in Table 2.

Table 2: Inversely estimated diffusivities α_s at the three field sites.

Period	Sites		
	T1 (mm^2s^{-1})	T2 (mm^2s^{-1})	TR (mm^2s^{-1})
∼June 24th	0.94	1.82	1.62
June 24th ∼Aug 9th	0.56	0.85	1.18
Aug 9th ∼	0.69	0.93	1.20

4 Results

The developed model of thaw depth in Eq. (3) is validated by comparing the modeled thaw depth and temperature profile with field observations at sites with different characteristics of seasonal freeze-thaw cycles.

4.1 Model Simulations

Flux G estimated using Eqs. (4) - (5) is in close agreement with the direct measurements at the study sites (Fig. 1), with the corresponding statistics summarized in Table 3. Accurate estimation of G provides reliable input of the proposed model of thaw depth. The corresponding soil heat flux estimated under the condition of the Stefan solution (A8) is also shown in Fig. 1. The Stefan model substantially overestimates G at the beginning of thawing and underestimates G in later stages, suggesting a substantial bias in the energy budget of the Stefan model. The effect of the energy budget imbalance on the thaw depth in the classical solution is discussed in detail below.

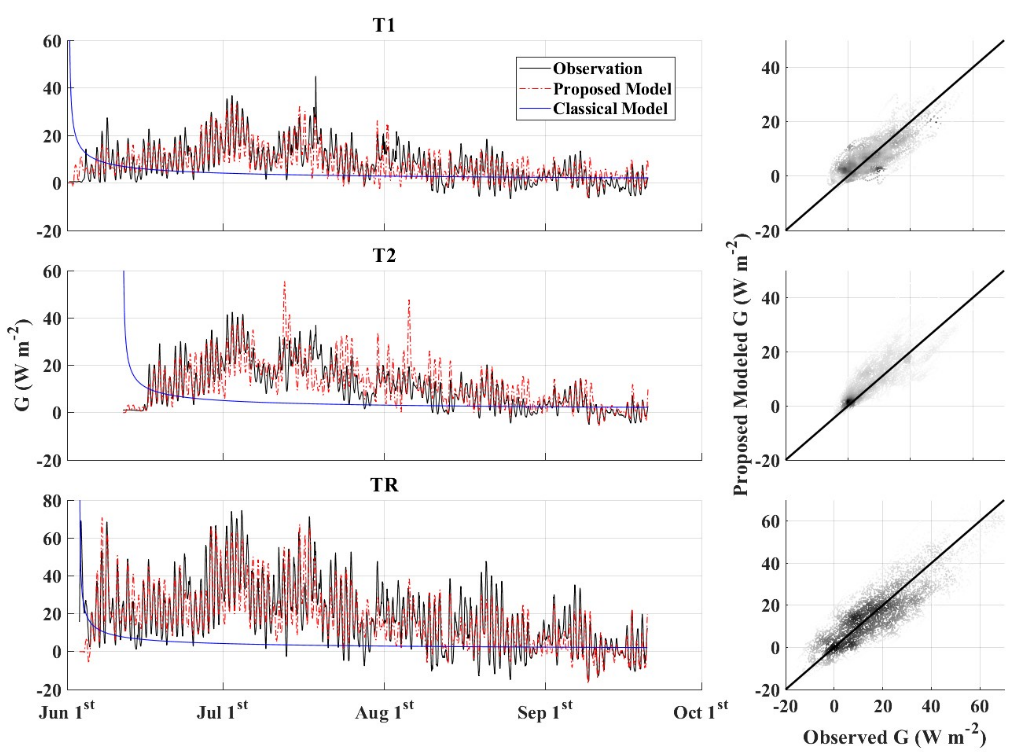

Figure 1: The proposed Eqs. (4) - (5) and classical Eq. (A8) modeled G vs. in-situ hourly observations at the three field study sites.

Table 3: Statistics of the modeled ('Model') soil heat flux compared to half-hourly observations ('OBS'). R^2 is the coefficient of determination; RMSE is the root mean square error.

Sites	Mean OBS (Wm^{-2})	Model		
		Mean (Wm^{-2})	R^2	RMSE (Wm^{-2})
T1	7.89	7.94	0.80	4.63
T2	10.5	11.9	0.80	6.21
TR	18.50	17.33	0.83	9.68

The modeled thaw depth $S(t)$ at the study sites is shown in Fig. 2. At T1 site, water content at 70 and 100 cm are observed to change almost simultaneously, indicating that the soil beyond 70 cm was not fully frozen during the pre-thawing season. It implies that the maximum depth of freezing at the T1 site is 70 cm. The occurrence of an unfrozen layer is possibly due to the isolated talik (Lunardini, 1981), which remained unfrozen during the winter season. At the T2 site, thawing starts on June 11th and the active layer thickness is larger than 1 m (the maximum monitoring depth). Thawing starts on May 31st and June 3rd at T1 and TR site, respectively.

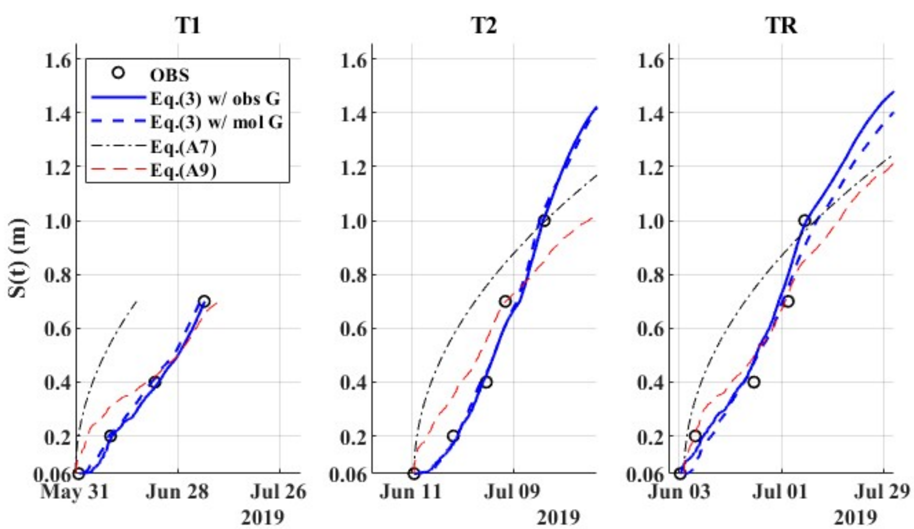

Figure 2: A comparison of the observed thaw depth ('OBS') with results of the two classical solution based models (Eq. (A7) and Eq. (A9)), and the proposed model (Eq. (3)) with non-gradient modeled ground heat flux (indicated as 'w/ mol G') and observed ground heat flux ('w/obs G') at the field study sites. The soil parameters remain unchanged below 1 m (the maximum measurement depth): $\kappa_L = 0.12$ W m^{-1} K^{-1} in Eq. (A7) and $T_s = 0.39$ °C the mean observed surface temperature of the thawing season.

Fig. 2 shows that both the observed and simulated thaw depths do not necessarily follow the square root of time evolution as described by the Stefan solution in Eq. (A7). The thawing rates at all sites accelerate during the period from mid-June to early

July, corresponding to the higher soil heat flux during this interval (Fig. 1). The increasing thawing rates in the middle of thawing season are also likely to be attributed to the lower ice content (e.g. Table 1, T2: 40 cm to 70 cm; TR: 20 cm to 40cm).

This comparison analysis highlights the crucial role of soil surface heat flux in modeling thaw depth at sub-seasonal time scales. As compared to the Stefan solution based models, the proposed model yields better performance with the time-varying soil surface heat flux input. The proposed model in Eq. (3) simulates $S(t)$ more accurately than the classical Stefan solution (A7) and the modified Stefan solution (A9) (Fig. 2). The two Stefan solution-based models in Eqs. (A7) and (A9) overestimate the thaw depth during the early stage of thawing. The biases of the Stefan solution-based models are arguably caused by the biases of ground heat flux input (Fig. 1). The discontinuous surface temperature boundary condition in the Stefan solution (A7) implies infinite initial ground heat flux, leading to the overestimation of thaw depth during the early stage of thawing. The steady-state surface temperature during the later stage of thawing leads to underestimated ground heat flux and hence the thaw depth. The developed solution in Eq. (A9) using a more realistic, time-varying surface temperature boundary condition outperforms estimation based on Eq. (A7) with the steady-state boundary condition of surface temperature. The modified Stefan solution intrinsically corresponds to the imbalanced surface energy budget caused by inaccurate ground heat flux input, i.e., thawing index cannot reflect the ground heat flux which satisfies surface energy budget.

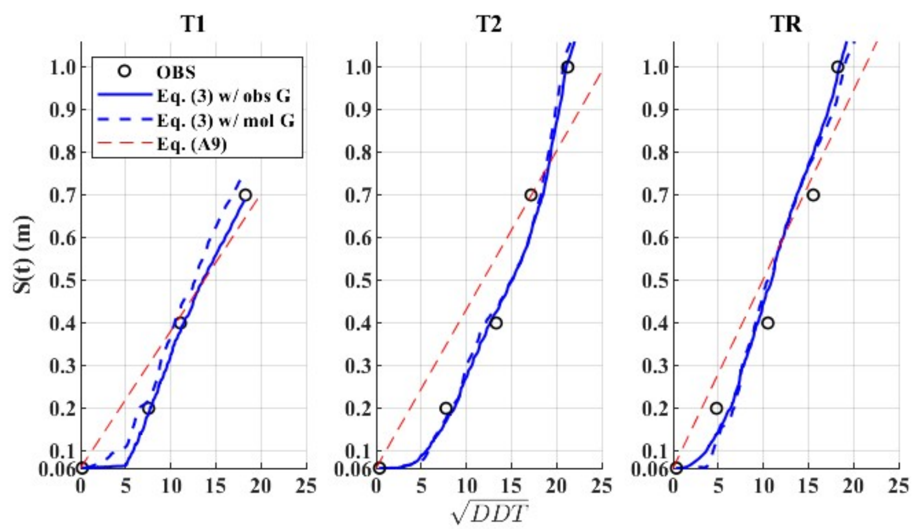

Figure 3: Modeled and observed S(t) vs. $DDT^{1/2}$ at the study sites.

Thaw depth $S(t)$ estimated using Eq. (A9) has evident biases as compared to $S(t)$ using Eq. (3) and observations (Fig. 2, Fig. 3). The thaw depth is underestimated when the thawing index is low. Due to the 'zero-curtain' effect (Outcalt et al., 1990), the top layer soil temperature remains close to the melting point during the early stage of thawing, i.e., ground heat flux is close to zero. The thawing index however is calculated using the cumulative air temperature, which implicitly yields a higher ground heat flux than what is implied by the nearly isothermal state of the top soil. The estimated constant b in Eq. (A9) is arguably partially responsible for the biases of the $S(t)$ solution based on the thawing index (K. M. Hinkel & Nicholas, 1995). Specifically, constant b in Eq. (A9) is estimated using temporally aggregated dynamics of thaw process, and does not represent the real-world effect of temporally and spatially varying ice content and soil thermal properties on the thawing rate.

4.2 Approximate Analytical Solution of Soil Temperature Profile

The time series of modeled and observed soil temperature profiles are shown in Fig. 4a to Fig. 4c. It is noticed that the modeled and observed soil temperature are in good agreement with maximum modeling errors less than 3°C. The soil temperature remaining at around 0°C suggests that the thawing front has not yet reached the corresponding depth. It is noticed that the observed soil temperature profile remains at 0°C, supporting the assumption of isothermal temperature profile before thawing starts. Meanwhile, the observed soil temperature at the T2 site started to increase on Jun 13th, before thawing front reaches 20 cm on Jun 24th (Fig. 4b), which is inconsistent with the volumetric water content measurement. This discrepancy is likely caused by the vertical flow of liquid water creating additional advective heat source which is not accounted in the proposed model. That explains the under-estimated soil temperature during the first 20 days. Relatively large modeling error for T1 site occurs after thawing front has reached 70 cm on July 5th (Fig. 4a) due to the presence of talik, implying that the thermal energy reaching the thaw front led to changing soil temperature instead of water phase change. Thus, Eq. (3) does not hold when talik appears due to the fact that no more energy needed for phase change at thawing front. For T2 and TR sites, no talik was detected during the observation period. The modeling error is primarily observed after the thaw depth exceeds the maximum measurement depth. Beyond the point, the soil properties are assumed to be the same as properties at the maximum measurement depth and remain to be constant, regardless of the actual depth, which does not accurately reflect the real conditions.

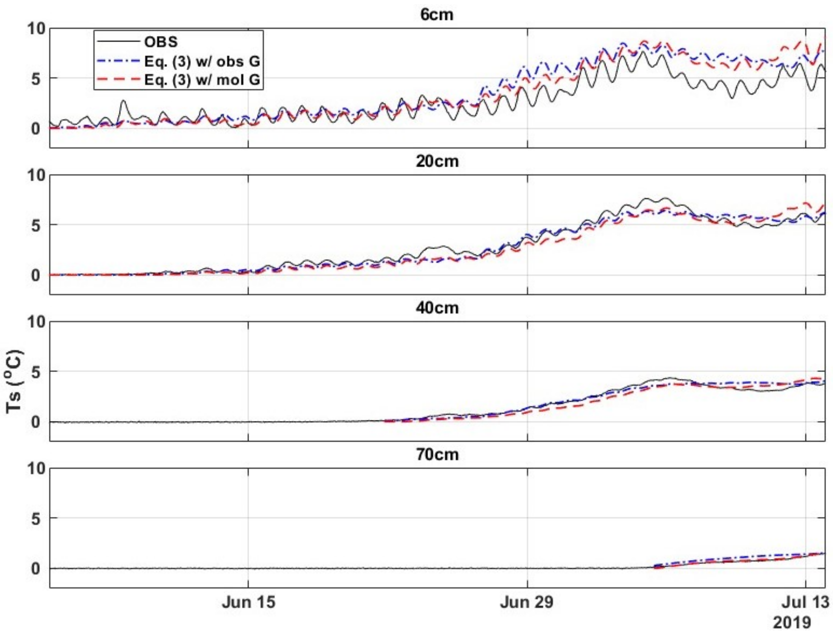

(a) A comparison of modeled and observed hourly soil temperature at T1 site. Soil depth is indicated in the subplot titles.

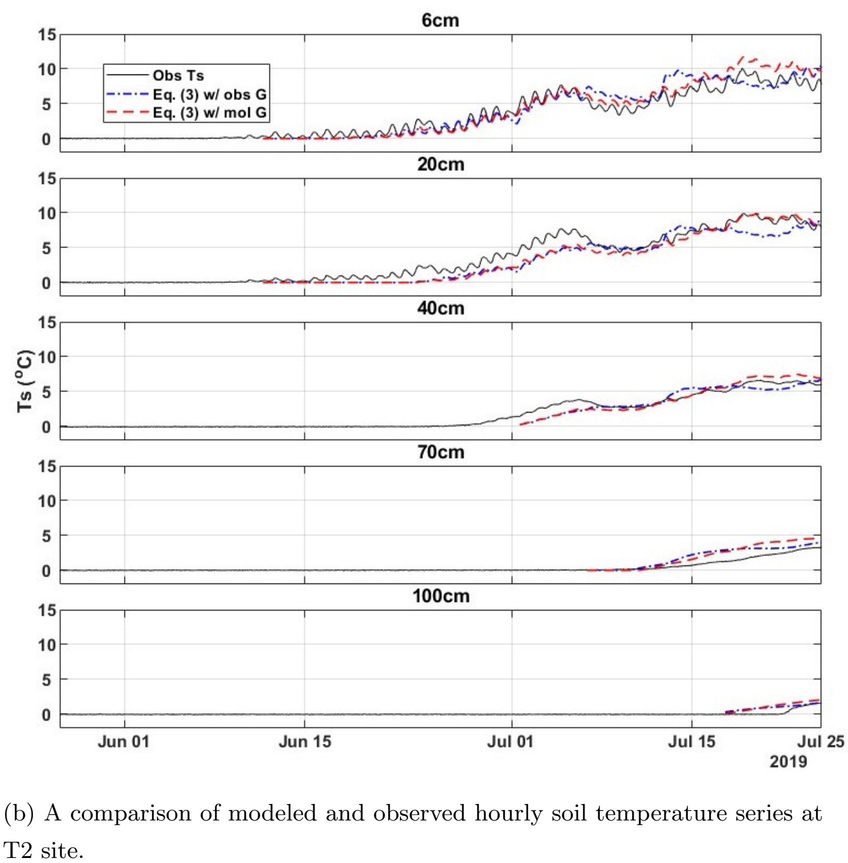

(b) A comparison of modeled and observed hourly soil temperature series at T2 site.

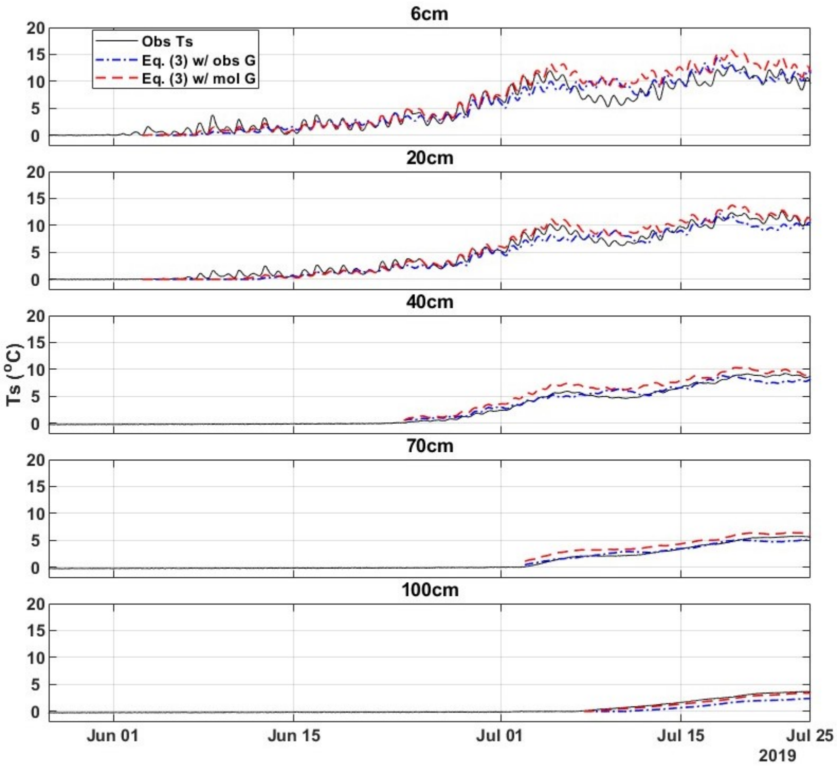

(c) A comparison of modeled and observed hourly soil temperature at TR site.

Figure 4: Comparison of modeled and observed soil temperature

270 A summary of statistical comparison between the observed and modeled soil temperature time series is shown in Table 4. The proposed model effectively estimates soil temperature profile with R^2 higher than 0.68 (mostly higher than 0.9) and RMSE ≤ 1.73 °C (mostly lower than 1 °C). As compared to the observed ground heat flux G, the modeled G is shown to yield better performance in estimating soil temperature profile. That is caused by the fact that measurement of heat flux plate could be influenced by various factors such as and soil topography. And the non-gradient model has been proven to be able to effectively reflect the surface energy budget with more reliable measurements (El Sharif et al., 2019).

Table 4: The coefficient of determination (R^2) and root mean square error (RMSE) of modeled hourly soil temperature series. 'w/ Obs G' are calculated by using soil heat flux observed in Eq. (3); 'w/ Mol G' are calculated by using soil heat flux modeled by using Eq. (3). 'NA' for T1 site indicates that ice was not present at the depth of 100 cm at T1 site.

Site		T1		T2		TR	
Depth		R^2	RMSE (°C)	R^2	RMSE (°C)	R^2	RMSE (°C)
6cm	w/ Obs G	0.87	1.50	0.88	1.25	0.90	1.36
	w/ Mol G	0.92	1.32	0.97	1.08	0.97	1.73
20cm	w/ Obs G	0.96	0.50	0.90	1.44	0.95	1.01
	w/ Mol G	0.96	0.61	0.94	1.20	0.99	0.92
40cm	w/ Obs G	0.94	0.35	0.78	0.93	0.95	0.70
	w/ Mol G	0.94	0.44	0.96	0.87	0.98	1.23
70cm	w/ Obs G	0.88	0.34	0.82	0.99	0.96	0.44
	w/ Mol G	0.97	0.08	0.95	1.13	0.99	1.02
100cm	w/ Obs G	NA		0.74	0.68	0.98	1.03
	w/ Mol G			0.68	0.82	0.99	0.31

5 Conclusions

The proposed physically based analytical model in Eq. (3) is able to simulate the sub-seasonal active layer thaw depth driven by temporally changing ground heat flux. Due to the high nonlinearity caused by the thawing front as a moving boundary, a superimposed temperature correction term is applied in the energy conservation equation and to keep the thawing front soil temperature at melting point. As compared to the Stefan solution based models, whose input is air temperature and since they cannot fully reflect soil energy budget, the proposed model with ground heat flux as input leads to more accurate simulation of thaw depth. When in situ observed ground heat flux is not available, non-gradient models such as the one in Eq. (4) can yield reasonable estimation of the soil surface energy budget and thus G. Such a derived ground heat flux is shown to have lower estimation errors than the sampling errors of direct measurements of ground heat flux. The approximate analytical solution of soil temperature profile is in close agreement with in-situ observations, which is superior to the Stefan solution based models. These findings justify an application of the proposed models for the simulation of thaw depth at the regional scales – a topic of follow-up studies.

Appendix A Two-phase Stefan problem, Neumann similarity solution, and modified Stefan solution

The classical Neumann solution of the two-phase Stefan problem for the process of thaw can be represented by the heat conduction equation for a one-dimensional semi-infinite medium (e.g. water) with a moving thawing front $S(t)$ (e.g. Alexiades, 1992),

$$\begin{gathered}\frac{\partial T(x,t)}{\partial t} = \alpha_L \frac{\partial^2 T(x,t)}{\partial x^2},\ 0 \le x \le S(t) \\ T(x,t) = T_m,\ S(t) \le x < \infty, t \ge 0\end{gathered} \tag{A1}$$

where $S(t)$ is the thaw depth, $T(x,t)$ is the temperature profile at time t, x is the location coordinate with the surface at $x = 0$, T_m (0°C) is the thawing temperature, and

α_L is the thermal diffusivity ($\mathrm{m^2s^{-1}}$) of liquid medium subject to the initial and boundary conditions

$$\begin{aligned} T(x,0) &= T_m \\ T(0,t) &= T_s > T_m,\ t > 0 \end{aligned} \tag{A2}$$

where T_s is the surface temperature, which is assumed to be constant. The Stefan condition at the moving boundary, which states that the rate of energy arriving at the front by heat conduction is equal to the rate of heat absorbed by the ice in the soil as its heat of melting, is represented by

$$\begin{aligned} \rho_s \lambda_f \frac{dS(t)}{dt} &= -\kappa_L \frac{\partial T(S(t),t)}{\partial x} \\ S(0) &= 0 \end{aligned} \tag{A3}$$

where κ_L is the thermal conductivity of liquid medium, ρ_s is the density of solid medium, and λ_f is the latent heat of fusion. The Neumann similarity solution is given as

$$\begin{aligned} T(x,t) &= T_s - (T_s - T_m)\frac{erf\left(\frac{x}{2\sqrt{\alpha_L t}}\right)}{erf(\gamma)} \\ S(t) &= 2\gamma\sqrt{\alpha_L t} \end{aligned} \tag{A4}$$

where erf is the error function and γ is the solution of the transcendental equation:

$$\frac{exp(-\gamma^2)}{erf(\gamma)} = \sqrt{\pi}\gamma\frac{\lambda_f}{C_L(T_s - T_m)} \tag{A5}$$

where C_L is the heat capacity of the liquid medium. For small γ, Eq. (A5) reduces to (e.g. Lunardini, 1981),

$$\gamma = \sqrt{\frac{C_L(T_s - T_m)}{2\lambda_f}} \tag{A6}$$

leading to the "Stefan solution",

$$S(t) = \sqrt{\frac{2\kappa_L(T_s - T_m)}{\lambda_f \rho_s}t} \tag{A7}$$

The corresponding ground heat flux is expressed as,

$$G = \frac{k(T_s - T_m)}{\sqrt{\pi\alpha_L}erf(\gamma)}\frac{1}{\sqrt{t}} \tag{A8}$$

A modified Stefan solution of thaw depth is expressed in terms of DDT (°C day), the cumulative number of degree-days above zero degree Celsius since the onset of thawing (K. M. Hinkel & Nicholas, 1995),

$$S(t) = b\sqrt{DDT} \equiv b\sqrt{\int_0^t \left[T_s(\tau) - T_m\right] d\tau}, T_s > T_m \tag{A9}$$

where b ($\mathrm{m^\circ C^{-1/2}day^{-1/2}}$) is assumed to be a constant fitting parameter, calculated from the best-fit line to the observations.

Appendix B Derivation of Eq.(3)

Based on Eq. 2, $T(S(t),t)$ can be expressed as:

$$T(S(t),t) = T_0 + \frac{1}{I_s\sqrt{\pi}}\int_0^t exp\left(-\frac{S^2}{4\alpha_s(t-\tau)}\right)\frac{G(\tau)}{\sqrt{t-\tau}}d\tau \tag{B1}$$

$T(S(t))$ is then considered as the temperature correction term to keep thawing front temperature remain at melting point. Applying the temperature correction term in the energy conservation equation Eq. (1) leads to

$$\int_0^t G(\tau)d\tau = \int_0^{S(t)} C_s \left[\frac{1}{I_s\sqrt{\pi}}\left[\int_0^t exp\left(-\frac{x^2}{4\alpha_s(t-\tau)}\right)\frac{G(\tau)}{\sqrt{t-\tau}}d\tau - \int_0^t exp\left(-\frac{S^2}{4\alpha_s(t-\tau)}\right)\frac{G(\tau)}{\sqrt{t-\tau}}d\tau\right]\right]dx + \lambda_f\rho_i\int_0^{S(t)}\theta_i(x)dx \tag{B2}$$

As $I_s = C_s\sqrt{\alpha_s}$, Eq. (B2) can be expressed as

$$\int_0^t G(\tau)d\tau = \int_0^{S(t)}\left[\frac{1}{\sqrt{\alpha_s\pi}}\left[\int_0^t exp\left(-\frac{x^2}{4\alpha_s(t-\tau)}\right)\frac{G(\tau)}{\sqrt{t-\tau}}d\tau\right]\right]dx + \lambda_f\rho_i\int_0^S(t)\theta_i dx - \int_0^{S(t)}\left[\frac{1}{\sqrt{\alpha_s\pi}}\left[\int_0^t exp\left(-\frac{S^2}{4\alpha_s(t-\tau)}\right)\frac{G(\tau)}{\sqrt{t-\tau}}d\tau\right]\right]dx \tag{B3}$$

Eq. (B3) can be simplified by moving the first term on the right hand side to left hand side

$$\int_0^t erfc\left(\frac{S}{2\sqrt{\alpha_s(t-\tau)}}\right)G(\tau)d\tau = \lambda_f\rho_i\int_0^{S(t)}\theta_i(x)dx - \int_0^{S(t)}\left[\frac{1}{\sqrt{\alpha_s\pi}}\left[\int_0^t exp\left(-\frac{S^2}{4\alpha_s(t-\tau)}\right)\frac{G(\tau)}{\sqrt{(t-\tau)}}d\tau\right]\right]dx \tag{B4}$$

The second term on the right hand side in Eq. (B4) can be simplified through interchange of the order of integration and we can finally get the expression for the proposed model

$$\int_0^t G(\tau)\left[erfc\left(\frac{S(\tau)}{2\sqrt{\alpha_s(t-\tau)}}\right) + \frac{S(\tau)}{\sqrt{\alpha_s\pi(t-\tau)}}exp\left(-\frac{S^2(\tau)}{4\alpha_s(t-\tau)}\right)\right]d\tau = \lambda_f\rho_i\int_0^{S(t)}\theta_i(x)dx \tag{B5}$$

Eq. (B5) is the proposed equation. It is an implicit nonlinear integral equation that must be solved numerically.

Acknowledgments

This research is sponsored by the National Science Foundation (NSF) Office of Polar Programs grants 1724633 (Georgia Tech), 1725654, 2139432, and 2126792 (University of Michigan) and 1724868 (Kansas State University). V. Ivanov and V. Mazepa acknowledge the support from project RUB1-7032-EK-11 funded by the U.S. Civilian Research & Development Foundation. V. Ivanov was also partly supported by the NSF Navigating the New Arctic Program grants 1928014 and 2126792. V. Mazepa acknowledges the partial support from grant RFBR-19-05-00756 from the Russian Foundation for Basic Research. All authors are extremely grateful for the generous support of data collection program by the Arctic Research Station, Plant and Animal Ecology Institute, the Russian Academy of Sciences, the Urals Branch, Russia. We wholeheartedly thank the staff of the station Yuriy Trubnikov, V. Osokin, G. Popov, and V. Shtro for their technical and logistical support and extensive fieldwork.

References

ACIA. (2004). *Impacts of a warming arctic-arctic climate impact assessment.*

Alexiades, V. (1992). *Mathematical modeling of melting and freezing processes.* CRC Press.

Anisimov, O. A., Shiklomanov, N. I., & Nelson, F. E. (1997). Global warming and active-layer thickness: results from transient general circulation models. *Global and Planetary Change*, *15*(3-4), 61–77.

Bekryaev, R. V., Polyakov, I. V., & Alexeev, V. A. (2010). Role of polar amplification in long-term surface air temperature variations and modern arctic warming. *Journal of Climate*, *23*(14), 3888–3906.

Brown, J., Hinkel, K. M., & Nelson, F. (2000). The circumpolar active layer monitoring (calm) program: research designs and initial results. *Polar geography*, *24*(3), 166–258.

Bui, M. T., Lu, J., & Nie, L. (2020). A review of hydrological models applied in the permafrost-dominated arctic region. *Geosciences*, *10*(10), 401.

Carslaw, H. S., & Jaeger, J. C. (1947). Conduction of heat in solids. *Conduction of heat in solids*.

Chapin, F., Sturm, M., Serreze, M., McFadden, J., Key, J., Lloyd, A., … Rupp, T. (2005). Coauthors, 2005: Role of land-surface changes in arctic summer warming. *Science*, *310*(5748), 657–660.

Crank, J. (1975). *The mathematics of diffusion, oxford university press.* London.

Crate, S., Ulrich, M., Habeck, J. O., Desyatkin, A. R., Desyatkin, R. V., Fedorov, A. N., … others (2017). Permafrost livelihoods: A transdisciplinary review and analysis of thermokarst-based systems of indigenous land use. *Anthropocene*, *18*, 89–104.

El Sharif, H., Zhou, W., Ivanov, V., Sheshukov, A., Mazepa, V., & Wang, J. (2019). Surface energy budgets of arctic tundra during growing season. *Journal of Geophysical Research: Atmospheres*, *124*(13), 6999–7017.

Evans, S. G., & Ge, S. (2017). Contrasting hydrogeologic responses to warming in permafrost and seasonally frozen ground hillslopes. *Geophysical Research Letters*, *44*(4), 1803–1813.

Flerchinger, G. N. (2000). The simultaneous heat and water (shaw) model: Technical documentation. *Northwest Watershed Research Center USDA Agricultural Research Service, Boise, Idaho*, *910*.

Frauenfeld, O. W., Zhang, T., & Mccreight, J. L. (2007). Northern hemisphere freezing/thawing index variations over the twentieth century. *International Journal of Climatology: A Journal of the Royal Meteorological Society*, *27*(1), 47–63.

Gao, J., Xie, Z., Wang, A., Liu, S., Zeng, Y., Liu, B., … Xie, J. (2019). A new frozen soil parameterization including frost and thaw fronts in the community land model. *Journal of Advances in Modeling Earth Systems*, *11*(3), 659–679.

Hinkel, K., Paetzold, F., Nelson, F., & Bockheim, J. (2001). Patterns of soil temperature and moisture in the active layer and upper permafrost at barrow, alaska: 1993–1999. *Global and Planetary Change*, *29*(3-4), 293–309.

Hinkel, K. M., & Nicholas, J. R. (1995). Active layer thaw rate at a boreal forest site in central alaska, usa. *Arctic and Alpine Research*, *27*(1), 72–80.

Ivanov, V. Y., Sheshukov, A. Y., Wang, J., El Sharif, H. A., Liu, D., Mazepa, V., … Sokolov, A. (2018). Changes in surface processes due to tree expansion into tundra, polar urals, russia. In *Agu fall meeting abstracts* (Vol. 2018, pp. A53I–2605).

Jorgenson, M. T., Shur, Y. L., & Pullman, E. R. (2006). Abrupt increase in permafrost degradation in arctic alaska. *Geophysical Research Letters*, *33*(2).

Kudryavtsev, V., Garagulya, L., Melamed, V., et al. (1977). *Fundamentals of frost forecasting in geological engineering investigations (osnovy merzlotnogo prognoza pri inzhenerno-geologicheskikh issledovaniyakh)* (Tech. Rep.). COLD REGIONS RESEARCH AND ENGINEERING LAB HANOVER NH.

Ladanyi, B., & Andersland, O. (2004). *Frozen ground engineering.* Wiley.

Li, X., & Koike, T. (2003). Frozen soil parameterization in sib2 and its validation with game-tibet observations. *Cold Regions Science and Technology*, *36*(1-3), 165–182.

Lunardini, V. J. (1981). *Heat transfer in cold climates.* Van Nostrand Reinhold Company.

Mamode, M. (2013). Two phase stefan problem with boundary temperature condi-

tions: An analytical approach. *SIAM Journal on Applied Mathematics*, *73*(1), 460–474.
McGaw, R., SI, O., et al. (1978). Thermal properties and regime of wet tundra soils at barrow, alaska.
Miller, R. (1980). Freezing phenomena in soil. d. hillel (ed.) applications of soil physics. academic press, new york. *Freezing phenomena in soils. In D. Hillel (ed.) Applications of soil physics. Academic Press, New York.*.
Nelson, F., Outcalt, S., Goodwin, C., & Hinkel, K. (1985). Diurnal thermal regime in a peat-covered palsa, toolik lake, alaska. *Arctic*, 310–315.
Nelson, F., Shiklomanov, N., Mueller, G., Hinkel, K., Walker, D., & Bockheim, J. (1997). Estimating active-layer thickness over a large region: Kuparuk river basin, alaska, usa. *Arctic and Alpine Research*, *29*(4), 367–378.
Obu, J., Westermann, S., Bartsch, A., Berdnikov, N., Christiansen, H. H., Dashtseren, A., … others (2019). Northern hemisphere permafrost map based on ttop modelling for 2000–2016 at 1 km2 scale. *Earth-Science Reviews*, *193*, 299–316.
Ochsner, T. E., & Baker, J. M. (2008). In situ monitoring of soil thermal properties and heat flux during freezing and thawing. *Soil Science Society of America Journal*, *72*(4), 1025–1032.
Oelke, C., Zhang, T., Serreze, M. C., & Armstrong, R. L. (2003). Regional-scale modeling of soil freeze/thaw over the arctic drainage basin. *Journal of Geophysical Research: Atmospheres*, *108*(D10).
Oleson, K., Lawrence, D. M., Bonan, G. B., Drewniak, B., Huang, M., Koven, C. D., & Yang, Z.-L. (2013). *Technical description of version 4.5 of the community land model (clm)* (Tech. Rep. Nos. NCAR/TN-503+STR). doi: 10.5065/D6RR1W7M
Outcalt, S. I., Nelson, F. E., & Hinkel, K. M. (1990). The zero-curtain effect: Heat and mass transfer across an isothermal region in freezing soil. *Water Resources Research*, *26*(7), 1509–1516.
Overduin, P. P., & Kane, D. (2006). Frost boils and soil ice content: Field observations. *Permafrost and Periglacial Processes*, *17*(4), 291–307.
Overpeck, J., Hughen, K., Hardy, D., Bradley, R., Case, R., Douglas, M., … others (1997). Arctic environmental change of the last four centuries. *science*, *278*(5341), 1251–1256.
Patterson, D., & Smith, M. (1981). The measurement of unfrozen water content by time domain reflectometry: Results from laboratory tests. *Canadian Geotechnical Journal*, *18*(1), 131–144.
Riseborough, D., Shiklomanov, N., Etzelmüller, B., Gruber, S., & Marchenko, S. (2008). Recent advances in permafrost modelling. *Permafrost and Periglacial Processes*, *19*(2), 137–156.
Robinson, S. D., Turetsky, M. R., Kettles, I. M., & Wieder, R. K. (2003). Permafrost and peatland carbon sink capacity with increasing latitude. In *Proceedings of the 8th international conference on permafrost* (Vol. 2, pp. 965–970).
Romanovsky, V., & Osterkamp, T. (1997). Thawing of the active layer on the coastal plain of the alaskan arctic. *Permafrost and Periglacial processes*, *8*(1), 1–22.
Romanovsky, V. E., Smith, S. L., & Christiansen, H. H. (2010). Permafrost thermal state in the polar northern hemisphere during the international polar year 2007–2009: a synthesis. *Permafrost and Periglacial processes*, *21*(2), 106–116.
Schuur, E. A., McGuire, A. D., Schädel, C., Grosse, G., Harden, J. W., Hayes, D. J., … others (2015). Climate change and the permafrost carbon feedback. *Nature*, *520*(7546), 171–179.
Sellers, P., Randall, D., Collatz, G., Berry, J., Field, C., Dazlich, D., … Bounoua, L. (1996). A revised land surface parameterization (sib2) for atmospheric gcms.

part i: Model formulation. *Journal of climate*, *9*(4), 676–705.
Serreze, M., Walsh, J., Chapin, F., Osterkamp, T., Dyurgerov, M., Romanovsky, V., ... Barry, R. (2000). Observational evidence of recent change in the northern high-latitude environment. *Climatic change*, *46*, 159–207.
Streletskiy, D. A., Shiklomanov, N. I., & Nelson, F. E. (2012). Permafrost, infrastructure, and climate change: a gis-based landscape approach to geotechnical modeling. *Arctic, Antarctic, and Alpine Research*, *44*(3), 368–380.
Van Everdingen, R. (1998). *Multi-language glossary of permafrost and related ground-ice terms, revisado en mayo de 2005. national snow and ice data center/world data center for glaciology, boulder, co.*
Vuik, C. (1993). Some historical notes about the stefan problem.
Walvoord, M. A., & Kurylyk, B. L. (2016). Hydrologic impacts of thawing permafrost—a review. *Vadose Zone Journal*, *15*(6).
Wang, J., & Bras, R. (2011). A model of evapotranspiration based on the theory of maximum entropy production. *Water Resources Research*, *47*(3).
Wang, J., & Bras, R. L. (2009). A model of surface heat fluxes based on the theory of maximum entropy production. *Water resources research*, *45*(11).
Wang, Z.-H., & Bou-Zeid, E. (2012). A novel approach for the estimation of soil ground heat flux. *Agricultural and Forest Meteorology*, *154*, 214–221.
Yang, J., & Wang, Z.-H. (2014). Land surface energy partitioning revisited: A novel approach based on single depth soil measurement. *Geophysical Research Letters*, *41*(23), 8348–8358.
Yi, Y., Kimball, J. S., Chen, R. H., Moghaddam, M., Reichle, R. H., Mishra, U., ... Oechel, W. C. (2018). Characterizing permafrost active layer dynamics and sensitivity to landscape spatial heterogeneity in alaska. *The Cryosphere*, *12*(1), 145–161.

Fig1.jpg.

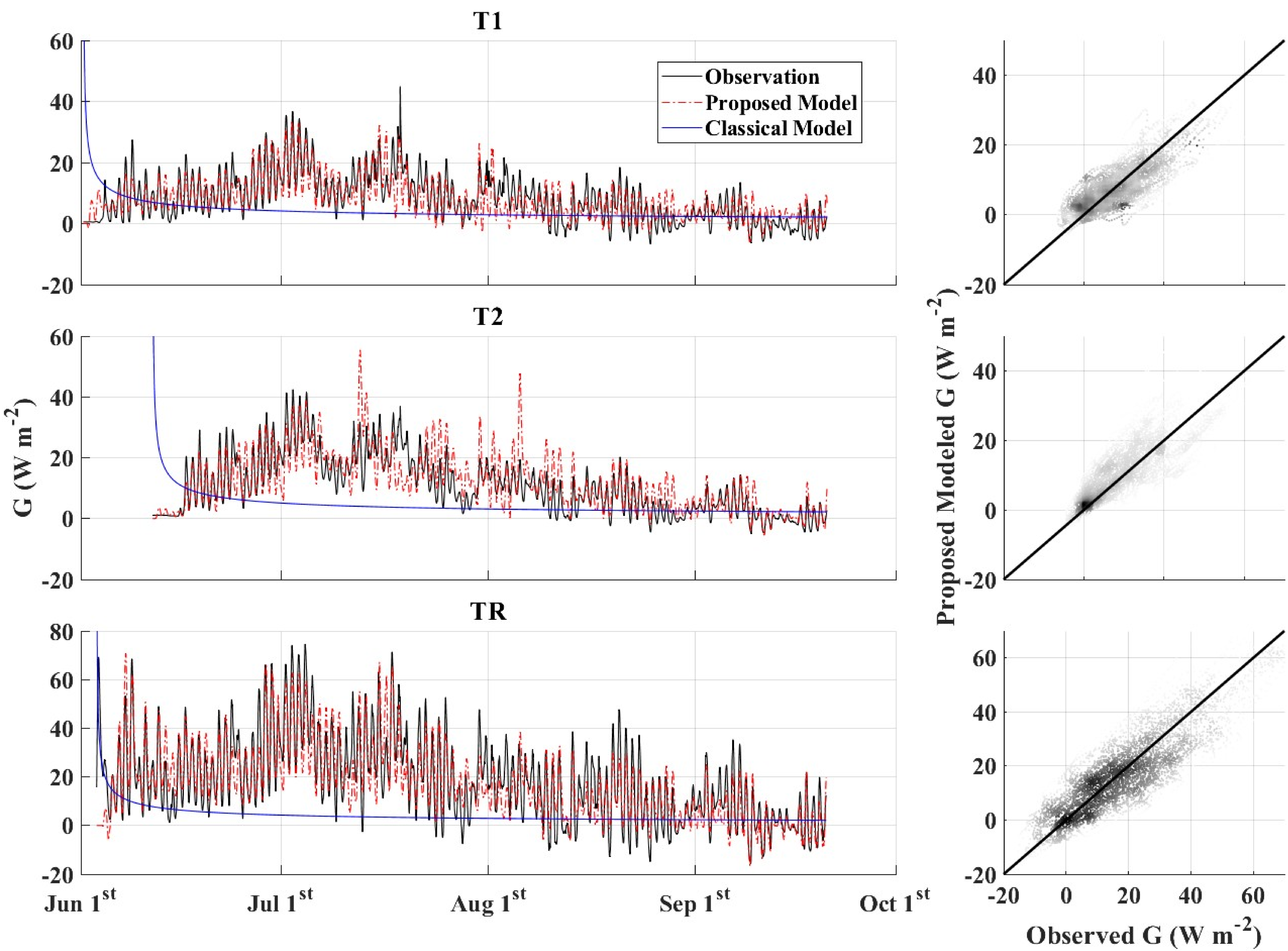
T1
T2
TR
Observation
Proposed Model
Classical Model
G (W m^{-2})
Jun 1st
Jul 1st
Aug 1st
Sep 1st
Oct 1st
Proposed Modeled G (W m^{-2})
Observed G (W m^{-2})

Fig2.jpg.

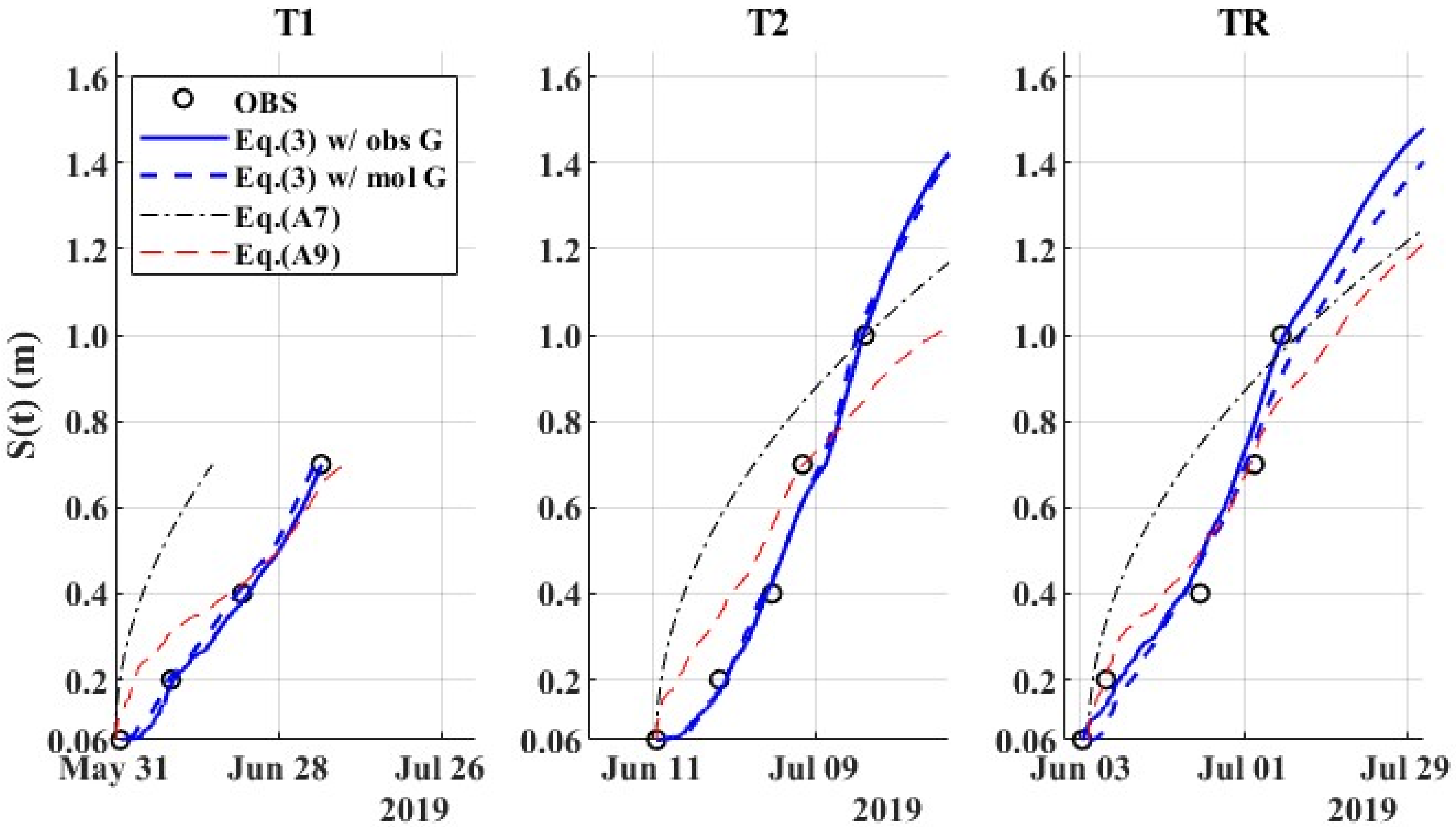
T1
T2
TR
OBS
Eq.(3) w/ obs G
Eq.(3) w/ mol G
Eq.(A7)
Eq.(A9)
S(t) (m)
1.6
1.4
1.2
1.0
0.8
0.6
0.4
0.2
0.06
May 31
Jun 28
Jul 26
Jun 11
Jul 09
Jun 03
Jul 01
Jul 29
2019

Fig3.jpg.

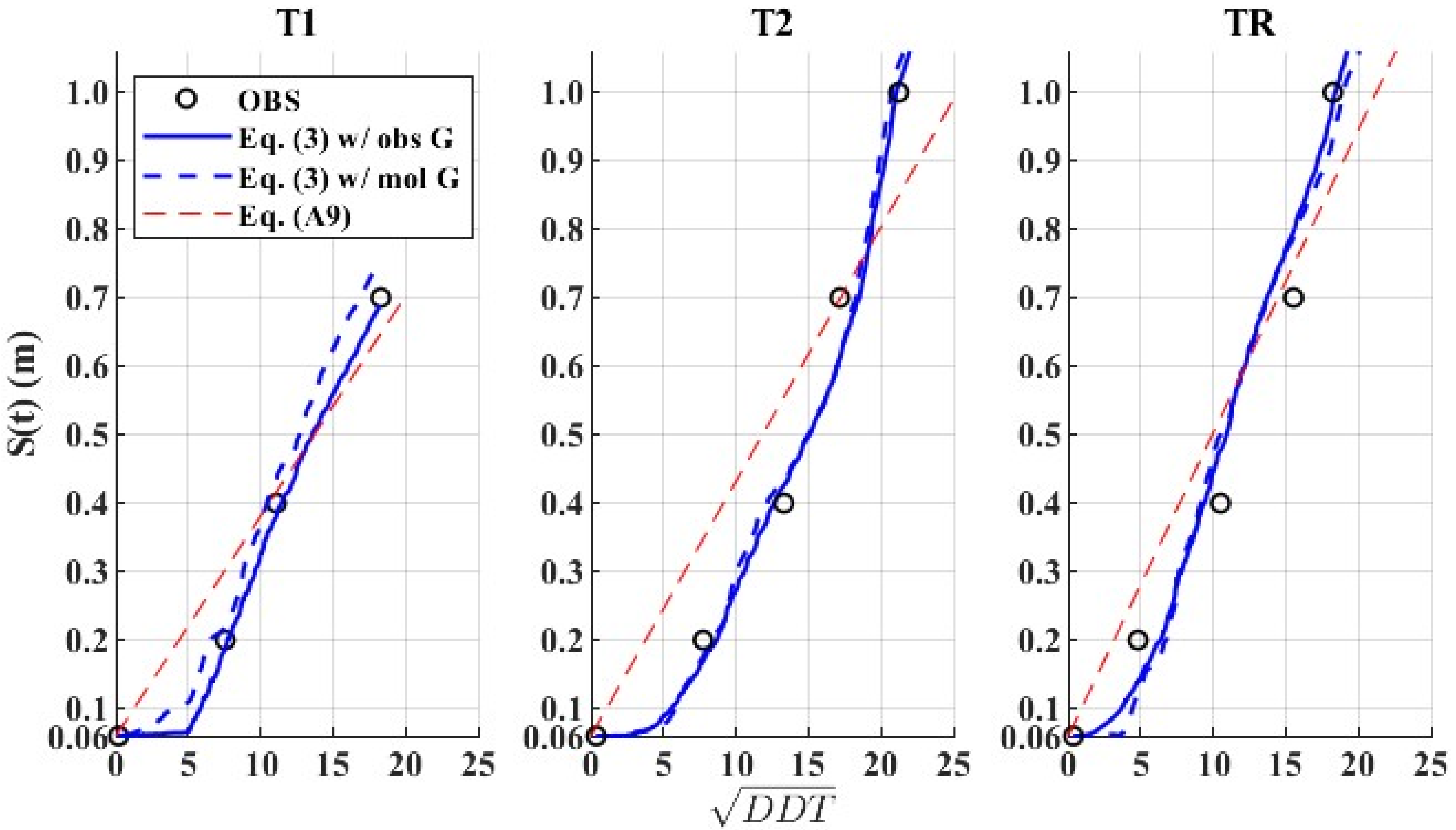

T1
T2
TR
OBS
Eq. (3) w/ obs G
Eq. (3) w/ mol G
Eq. (A9)
S(t) (m)
$\sqrt{DDT}$
0.06
0.1
0.2
0.3
0.4
0.5
0.6
0.7
0.8
0.9
1.0
0
5
10
15
20
25

Fig4_a.jpg.

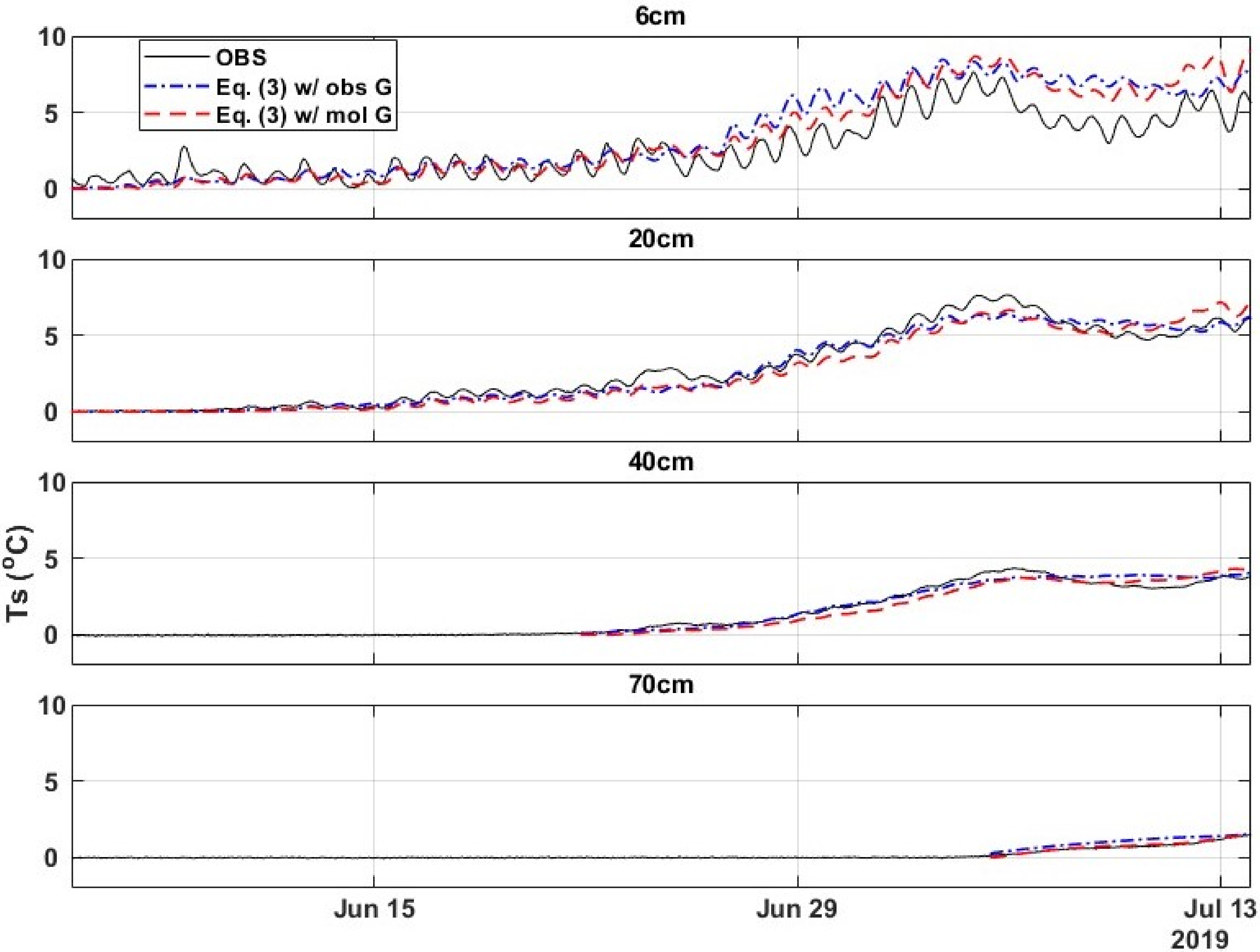

6cm
OBS
Eq. (3) w/ obs G
Eq. (3) w/ mol G
20cm
40cm
70cm
Ts (°C)
10
5
0
Jun 15
Jun 29
Jul 13
2019

Fig4_b.jpg.

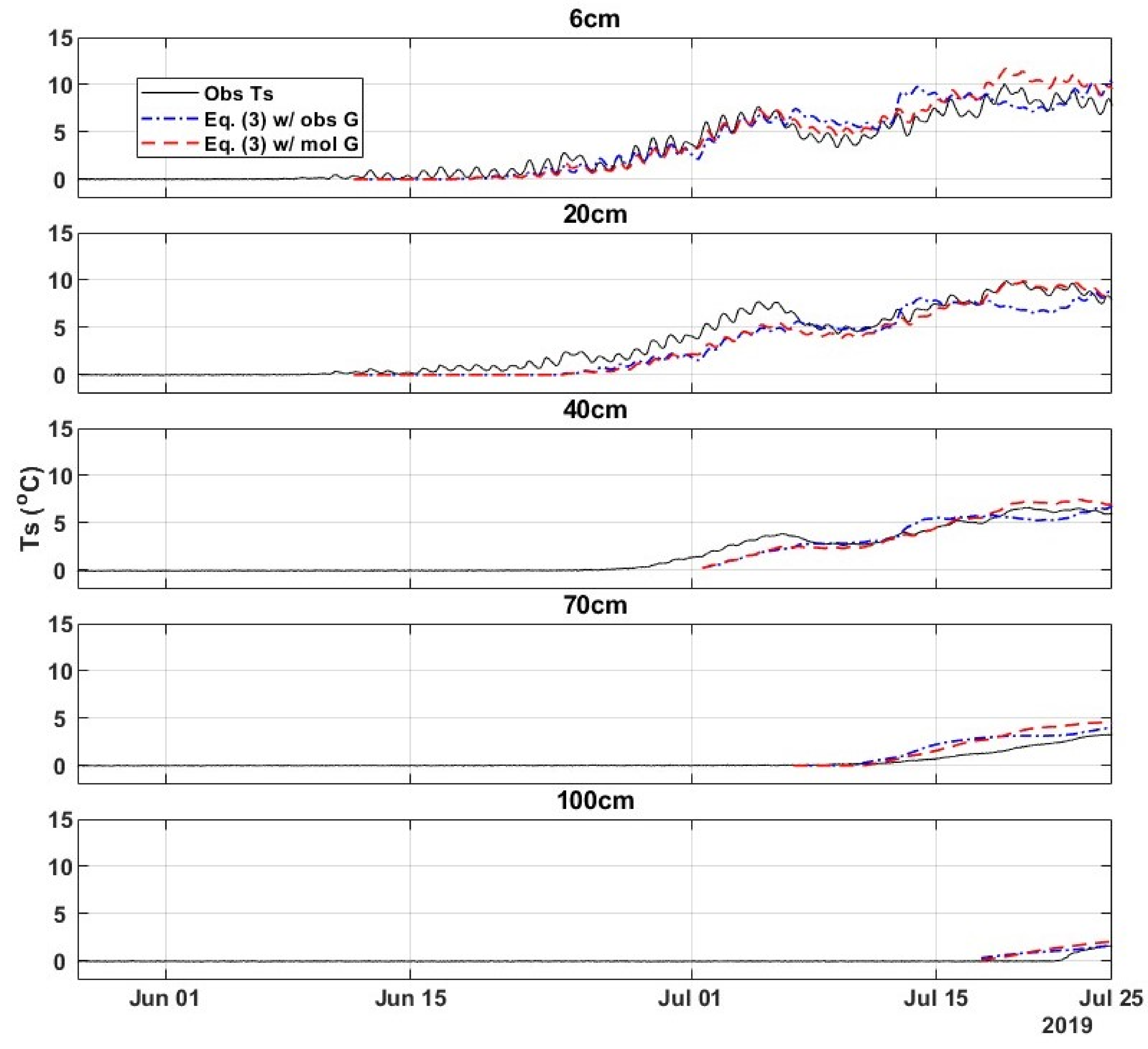
6cm
20cm
40cm
70cm
100cm
Obs Ts
Eq. (3) w/ obs G
Eq. (3) w/ mol G
Ts (°C)
15
10
5
0
Jun 01
Jun 15
Jul 01
Jul 15
Jul 25
2019

Fig4_c.jpg.

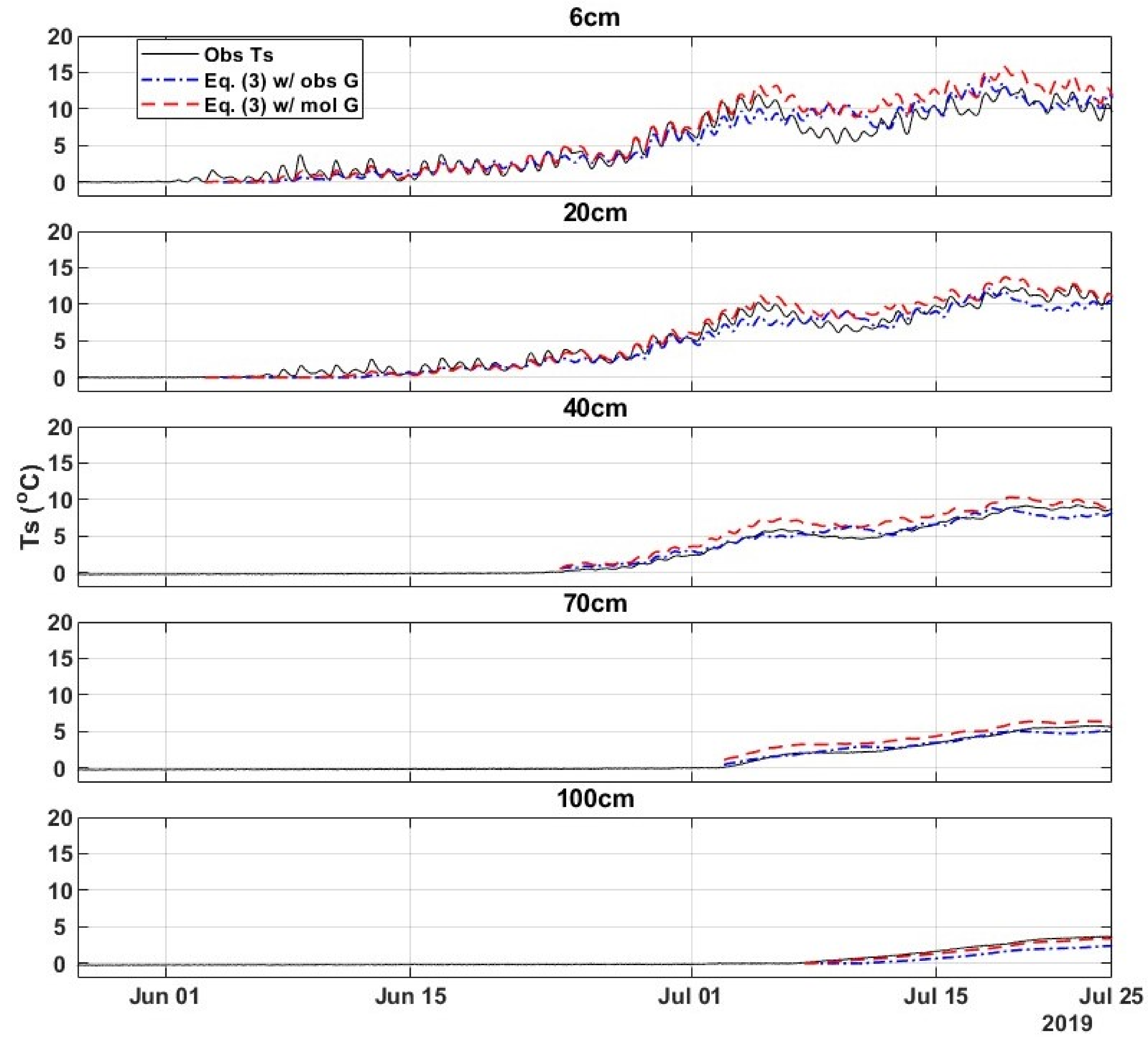

6cm
20cm
40cm
70cm
100cm
Obs Ts
Eq. (3) w/ obs G
Eq. (3) w/ mol G
Ts (°C)
0
5
10
15
20
Jun 01
Jun 15
Jul 01
Jul 15
Jul 25
2019